A Displacement Reconstruction Strategy for Long, Slender Structures from Limited Strain Measurements and Its Application to Underground Pipeline Monitoring

Mayank Chadha(✉) and Michael D. Todd

Department of Structural Engineering, University of California San Diego, La Jolla, CA 92093-0085, USA
machadha@eng.ucsd.edu

Abstract. In this paper, we discuss about reconstructing the global deformed shape of slender structures such as pipelines, tethers, or cables from a limited set of scalar surface strain measurements. We present a comprehensive approach that captures the effect of curvature, shear, torsion, and axial deformation. Our primary focus is to demonstrate the applicability of the approach to aid in damage detection algorithms. This theory utilizes Cosserat rod theory and exploit localized linearization approach that helps to obtain local basis function set for the displacement solution in director frame. The uniaxial strain vector and the surface strain for the Cosserat beam incorporating the above-mentioned effects are obtained and used to develop the reverse algorithm to reconstruct global shape of the structure. Error analysis due to noise in measured strain values is performed and results are discussed.

Keywords: Cosserat rod theory · Shape reconstruction · Local basis function · Director frame · Underground pipelines

1 Introduction

This paper discusses the formulation of global shape sensing algorithm that captures the effect of curvature, shear, torsion and axial deformation focusing on the applicability of the shape sensing methodology in civil structures. The theoretical framework for shape sensing using finite strain measurements are laid by the work of Todd et al. [1] and Chadha and Todd [2]. The formulation holds the Euler-Bernoulli rigid cross-section assumption primarily because Poisson's effect and warping of the cross-section are not the dominant effects in slender structures.

The global shape sensing of slender structures is desirable in many instances like pipelines, oil exploration, tethers, cables, and even non-civil applications like cardiac catheters, surgical tubing, and others. This theory is geometrically exact and fully nonlinear; hence it can capture large deformations. The mechanics developed for this problem is rooted to the work of Cosserat and Cosserat [3], Simo [4], Simo and Vu-Quoc [5], Iura and Atluri [6], and Reissner [7–9].

J.P. Conte et al. (eds.), *Experimental Vibration Analysis for Civil Structures*,
Lecture Notes in Civil Engineering 5, https://doi.org/10.1007/978-3-319-67443-8_27

As mentioned in [2], the distributed strain sensing may be grouped into non-contact and contact methods. The technique illustrated here assumes a contact sensing method. This technique focus on obtaining the local uniaxial surface strain measures through any type of multiplexed sensing approach, including fiber Bragg gratings (FBGs), Rayleigh backscatter, or conventional resistive strain gauges.

The remainder of the paper is arranged as follows: Sect. 2 briefs the kinematics of the problem, develops the surface strain measurement incorporating the aforementioned deformation effects, and presents a locally-exact solution basis on which a global deformed shape is built. Section 3 presents the application of the techniques to underground pipeline monitoring in case of seismic events. Section 4 culminates the discussion with conclusions and observations.

2 Kinematic Description

2.1 Geometry of the Beam-Midcurve and the Directors

We briefly discuss about the theoretical framework developed in [2] as a matter of completion. The global shape of the structure is defined by a midcurve (the locus of cross-sectional geometric centroids), and the director triad attached to the midcurve. Therefore, in a pure geometric sense, the problem is a single manifold problem with the arc length ξ_1 being the manifold parameter. We define the initial unstrained reference configuration by $\Omega_o \subset \mathbb{R}^3$. We assume that the initial shape is known (in which the strain gauges are attached to the object in a zero-strain state), which we assume is straight for simplicity. The geometric description of the configuration of the beam is same as defined in [2], which we shall briefly discuss.

We define an orthogonal frame $\{\mathbf{E_i}\}$. The domain of the beam is defined by the material point $\{\xi_1, \xi_2, \xi_3\}$, such that the origin of the frame $\{\mathbf{E_i}\}$ is at $\{\xi_i = 0\}$ with $i = 1, \ldots, 3$. Let L_o represent the length of midcurve in the undeformed reference state $\Omega_o \subset \mathbb{R}^3$, such that $\xi_1 \in [0, L_o]$. Any configuration of the structure is defined by the mid-curve. The position vector $\varphi(\xi_1) = \varphi_i \mathbf{E_i}$, parametrized by the undeformed arclength ξ_1, represents the midcurve. The orientation of any cross-section in the deformed configuration $\Omega \subset \mathbb{R}^3$ is defined by the set of orthogonal Cosserat director triad $\{\mathbf{d_i}(\xi_1)\}$, such that $\mathbf{d_i}(\xi_1) = d_{ij}(\xi_1)\mathbf{E_j}$. The vector $\mathbf{d}_1(\xi_1)$ is perpendicular to the cross-section and the vectors $\{\mathbf{d}_2(\xi_1), \mathbf{d}_3(\xi_1)\}$ spans the cross-section of the beam at ξ_1. We note that

$$\mathbf{d_i}(\xi_1) = \mathbf{Q}(\xi_1)\mathbf{E_i}. \tag{1}$$

Here, $\mathbf{Q}(\xi_1)$ represents family of orthogonal matrices that belongs to $SO(3)$ rotational groups. Hence, they satisfy $\mathbf{Q}\mathbf{Q}^{\mathrm{T}} = \mathbf{I}$ and $\det \mathbf{Q} = 1$. $\mathbf{Q}(\xi_1)$ being a curve on the manifold $SO(3)$, the tangent vector to this curve in $SO(3)$ is expressed as $\mathbf{Q}_{,\xi_1}$ that represents the tangent space of $SO(3)$. It can be easily obtained that $\mathbf{Q}_{,\xi_1}\mathbf{Q}^{\mathrm{T}} = \mathbf{K}(\xi_1)$ such that $\mathbf{K}(\xi_1)$ is the linear space of skew symmetric matrices. Therefore, there exists an axial vector $\boldsymbol{\kappa} = \bar{\kappa}_i \mathbf{d_i}$ associated with $\mathbf{K}(\xi_1)$ such that $\mathbf{K}(\xi_1)\mathbf{g} = \boldsymbol{\kappa} \times \mathbf{g}$. Here, $\mathbf{g} = \bar{g}\mathbf{d_i}$ represents any vector in $\mathbb{R}^3$. Therefore, from (1),

$$\mathbf{d}_{\mathbf{i},\xi_1} = \left(\mathbf{Q}_{,\xi_1}\mathbf{Q}^{\mathrm{T}}\right)\mathbf{d}_{\mathbf{i}} = \mathbf{K}\mathbf{d}_{\mathbf{i}} = \boldsymbol{\kappa} \times \mathbf{d}_{\mathbf{i}}. \tag{2}$$

The vector $\boldsymbol{\kappa} = \bar{\kappa}_i \mathbf{d}_{\mathbf{i}}$ represents a Darboux vector associated with the infinitesimal rotation tensor $\mathbf{K}$, parametrized by ξ_1. Equation (2) represents the differential equation that governs the evolution of the directors and hence the cross-sections.

To define the position vector $\boldsymbol{\varphi}$ and the governing differential equation corresponding to $\boldsymbol{\varphi}$, we define the following:

1. Let $\theta(\xi_1)$ and $\phi(\xi_1)$ represent the pitch and yaw angle of the mid-curve. We define another triad $\{\mathbf{T}, \mathbf{V}, \mathbf{H}\}$ that originates from the centroid of each cross-section such that the vector $\{\mathbf{T}, \mathbf{V}\}$ spans the pitch angle plane. The vector $\mathbf{T}(\xi_1)$ is the tangent vector to the midcurve. Thus, $\mathbf{H} = \mathbf{T} \times \mathbf{V}$. If there is no shearing in the beam, the triad $\{\mathbf{T}, \mathbf{V}, \mathbf{H}\}$ coincides with $\{\mathbf{d_i}\}$. The definition is made clear in the Fig. 1 below. Therefore,

$$\begin{bmatrix} \mathbf{T}(\xi_1) \\ \mathbf{V}(\xi_1) \\ \mathbf{H}(\xi_1) \end{bmatrix} = \begin{bmatrix} \cos\theta(\xi_1)\cos\phi(\xi_1) & \sin\theta(\xi_1) & \cos\theta(\xi_1)\sin\phi(\xi_1) \\ -\sin\theta(\xi_1)\cos\phi(\xi_1) & \cos\theta(\xi_1) & -\sin\theta(\xi_1)\sin\phi(\xi_1) \\ -\sin\phi(\xi_1) & 0 & \cos\phi(\xi_1) \end{bmatrix} \begin{bmatrix} \mathbf{E}_1 \\ \mathbf{E}_2 \\ \mathbf{E}_3 \end{bmatrix} = \mathbf{W}_1 \begin{bmatrix} \mathbf{E}_1 \\ \mathbf{E}_2 \\ \mathbf{E}_3 \end{bmatrix}. \tag{3}$$

2. Assume that the deformed arc length coordinate is given by s. The infinitesimal length of the undeformed mid-curve $\mathrm{d}\xi_1$ deforms to $\mathrm{d}s$ causing infinitesimal axial strain $e(\xi_1)$. If the object is subjected to shear and torsion, the orientation of the cross-section changes. The tangent vector is no longer perpendicular to the cross-section. The shearing effect is quantified by the angles $\gamma_{11}(\xi_1)$, $\frac{\pi}{2} - \gamma_{12}(\xi_1)$ and $\frac{\pi}{2} - \gamma_{13}(\xi_1)$ subtended by the directors $\mathbf{d}_1, \mathbf{d}_2$ and $\mathbf{d}_3$ with the tangent vector $\mathbf{T}(\xi_1) = \frac{\partial \boldsymbol{\varphi}}{\partial S}$, as shown in Fig. 1. Hence following relation can be noted:

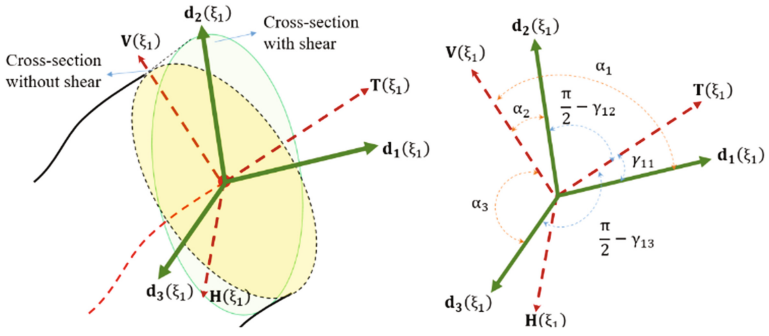

Fig. 1. Relationship between $\{\boldsymbol{d}_1, \boldsymbol{d}_2, \boldsymbol{d}_3\}$ and $\{\boldsymbol{T}, \boldsymbol{V}, \boldsymbol{H}\}$ material frame of reference (Color figure online)

$$e = \frac{\mathrm{d}s - \mathrm{d}\xi_1}{\mathrm{d}\xi_1}; \frac{\partial \xi_1}{\partial s} = \frac{1}{1+e},$$

$$\boldsymbol{\varphi}_{,s} \cdot \mathbf{d_i} = \frac{1}{1+e}\boldsymbol{\varphi}_{,\xi_1} \cdot \mathbf{d_i} = \left\{ \begin{matrix} \cos\gamma_{1i}, & \text{when } i = 1 \\ \sin\gamma_{1i}, & \text{when } i = 2,3 \end{matrix} \right\}. \tag{4}$$

Therefore,

$$\boldsymbol{\varphi}_{,\xi_1} = (1+e)\cos\gamma_{11}\mathbf{d}_1 + (1+e)\sin\gamma_{12}\mathbf{d}_2 + (1+e)\sin\gamma_{13}\mathbf{d}_3 = (1+e)\mathbf{T}. \tag{5}$$

3. It is necessary to define the parameters $\alpha_1(\xi_1)$, $\alpha_2(\xi_1)$ and $\alpha_3(\xi_1)$ as the angles subtended by the directors $\mathbf{d}_1, \mathbf{d}_2$ and $\mathbf{d}_3$ with the vector $\mathbf{V}$ respectively. This is done to define the relation between $\{\mathbf{T}, \mathbf{V}, \mathbf{H}\}$ and $\{\mathbf{d_i}\}$. Therefore, from the expression of tangent vector in Eq. (5), we can express,

$$\begin{bmatrix} \mathbf{T}(\xi_1) \\ \mathbf{V}(\xi_1) \\ \mathbf{H}(\xi_1) \end{bmatrix} = \mathbf{W}_2 \begin{bmatrix} \mathbf{d}_1 \\ \mathbf{d}_2 \\ \mathbf{d}_3 \end{bmatrix}. \tag{6}$$

Therefore, from Eqs. (3) and (5) we have,

$$\begin{bmatrix} \mathbf{d}_1 \\ \mathbf{d}_2 \\ \mathbf{d}_3 \end{bmatrix} = \mathbf{W}_2^{-1}\mathbf{W}_1 \begin{bmatrix} \mathbf{E}_1 \\ \mathbf{E}_2 \\ \mathbf{E}_3 \end{bmatrix}. \tag{7}$$

The component of the orthogonal tensor $\mathbf{Q}$ in Eq. (1) can be obtained from Eq. (7) in terms of the parameters $(\theta(\xi_1), \phi(\xi_1), \gamma_{1i}(\xi_1), \alpha_i(\xi_1))$ such that $\left[\mathbf{Q}^{\mathbf{T}}\right]_{\mathbf{d_i} \otimes \mathbf{E_i}} = \mathbf{W}_2^{-1}\mathbf{W}_1$. Note that the following orthogonality constrains hold,

$$|\mathbf{T}| = |\mathbf{V}| = |\mathbf{H}| = 1; \quad |\mathbf{T}|_{,\xi_1} = |\mathbf{V}|_{,\xi_1} = |\mathbf{H}|_{,\xi_1} = 0. \tag{8}$$

Therefore, the component of the Darboux vector can be obtained from the Eq. (2) in terms of the deformation parameters $(\theta(\xi_1), \phi(\xi_1), \gamma_{1i}(\xi_1), \alpha_i(\xi_1))$ and their derivatives, satisfying the constraints in Eq. (8). The expressions for $\bar{\kappa}_1, \bar{\kappa}_2$ and $\bar{\kappa}_3$ can be referred to Appendix A.1 in [2]. From Eqs. (2) and (5) we arrive at an important equation that governs the evolution of the system as,

$$\begin{bmatrix} \boldsymbol{\varphi}_{,\xi_1} \\ \mathbf{d}_{1,\xi_1} \\ \mathbf{d}_{2,\xi_1} \\ \mathbf{d}_{3,\xi_1} \end{bmatrix} = \begin{bmatrix} 0 & (1+e)\cos\gamma_{11} & (1+e)\sin\gamma_{12} & (1+e)\sin\gamma_{13} \\ 0 & 0 & \bar{\kappa}_3 & -\bar{\kappa}_2 \\ 0 & -\bar{\kappa}_3 & 0 & \bar{\kappa}_1 \\ 0 & \bar{\kappa}_2 & -\bar{\kappa}_1 & 0 \end{bmatrix} \begin{bmatrix} \boldsymbol{\varphi} \\ \mathbf{d}_1 \\ \mathbf{d}_2 \\ \mathbf{d}_3 \end{bmatrix}. \tag{9}$$

2.2 The Strain Vector

The position vector of any material point (ξ_1, ξ_2, ξ_3) in the deformed configuration Ω is given as,

$$\mathbf{R}(\xi_1, \xi_2, \xi_3) = \boldsymbol{\varphi}(\xi_1) + \xi_2 \mathbf{d}_2 + \xi_3 \mathbf{d}_3. \tag{10}$$

The strain vector ϵ for this problem is obtained as,

$$\epsilon = \sum_{\mathrm{i}=1}^{3} \left(\frac{\partial \mathbf{R}}{\partial \xi_i} - \mathbf{d_i} \right) = \frac{\partial \mathbf{R}}{\partial \xi_1} - \mathbf{d}_1. \tag{11}$$

Using Eq. (10), following expressions can be obtained,

$$\frac{\partial \mathbf{R}}{\partial \xi_i} = \begin{cases} \left(\boldsymbol{\varphi}_{,\xi_1} - \mathbf{d}_1 + \boldsymbol{\xi_2} \mathbf{d}_{2,\xi_1} + \boldsymbol{\xi_3} \mathbf{d}_{3,\xi_1} \right) + \mathbf{d}_1 = \boldsymbol{\epsilon} + \mathbf{d}_1, & \text{when } i = 1; \\ \mathbf{d_i}, & \text{when } i = 2, 3. \end{cases} \tag{12}$$

Equations (11) and (12) represent the fact that only the first component of any infinitesimal vector in the undeformed state Ω_o gets strained to $\boldsymbol{\epsilon} + \mathbf{d}_1$. Any vector on the cross-section plane of the beam rotates and is not strained. Using Eqs. (9), (11) and (12), the expression of strain vector in terms of deformation parameters $(e, \gamma_{1i}, \bar{\kappa}_i)$ becomes

$$\boldsymbol{\epsilon} = \{((1+e)\cos\gamma_{11} - 1) - \xi_2\bar{\kappa}_3 + \bar{\kappa}_2\xi_3\}\mathbf{d}_1 + \{(1+e)\sin\gamma_{12} - \bar{\kappa}_1\xi_3\}\mathbf{d}_2 + \{(1+e)\sin\gamma_{13} + \bar{\kappa}_1\xi_2\}\mathbf{d}_3. \tag{13}$$

Consider a point q on the surface of the undeformed section on which the strain gauge is attached. If p represent the midcurve point, the vector $\mathbf{r}_{pq} = \xi_2\mathbf{E}_2 + \xi_3\mathbf{E}_3$ represents the position vector of the strain gauge with respect to the midcurve for the given section. We represent the magnitude of the vector $\mathbf{r}_{pq}$ as $r = \sqrt{\xi_2^2 + \xi_3^2}$. The vector $\mathbf{r}_{pq}$ makes an angle σ with $\mathbf{E}_2$. Hence, $\xi_2 = r\cos\sigma$ and $\xi_3 = r\sin\sigma$.

To find the scalar value of strain in the strain gauge, we need the orientation of the strain gauge. If μ is the angle subtended by the strain gauge with the vector $\mathbf{E}_1$ in undeformed configuration or $\mathbf{d}_1$ in the deformed configuration, the direction of the strain gauge in the deformed configuration is obtained as $\mathbf{n} = \cos\mu\mathbf{d}_1 - \sin\mu\sin\sigma\mathbf{d}_2 + \sin\mu\cos\sigma\mathbf{d}_3$ as obtained in [2]. We define the following strain parameters

$$S_1 = ((1+e)\cos\gamma_{11} - 1); S_2 = (1+e)\sin\gamma_{12}; S_3 = (1+e)\sin\gamma_{13}$$

$$S_4 = r\bar{\kappa}_1; S_5 = r\bar{\kappa}_2; S_6 = r\bar{\kappa}_3;$$

$$e = \sqrt{(S_1+1)^2 + S_2^2 + S_3^2} - 1. \tag{14}$$

The scalar strain is obtained as a function of the strain parameters S_i using Eqs. (13) and (14) as

$$\begin{aligned}\varepsilon &= \boldsymbol{\epsilon} \cdot \mathbf{n} \\ &= \{S_1 - \cos\sigma \cdot S_6 + \sin\sigma \cdot S_5\}\cos\mu \\ &\quad - \{S_2 - \sin\sigma \cdot S_4\}\sin\mu\,\sin\sigma + \{S_3 + \cos\sigma \cdot S_4\}\sin\mu\,\cos\sigma\end{aligned} \tag{15}$$

2.3 Solution Approach

We demonstrate the solution for the circular section such that $|\mathrm{r}_{pq}|$ is constant for all the strain gauges. The solution may be easily extended to the non-circular section based on the theory discussed above. Solution of Eq. (9) requires 6 strain parameters $(S_1, \ldots, S_6)$. This requires 6 strain gauges per cross-sections. Equation (15) can then be inverted to obtain the strain parameters $(S_1, \ldots, S_6)$. To obtain the approximate structure, we discretize the object into N segments. At the n^{th} discretized cross-section $\left(\xi_1 = \xi_{1_n}\right)$, we attach 6 strain gauges with angles $\sigma_{n,m}$, at a distance of $r_{n,m} = r$ from the centroid, where $m = 1, \ldots, 6$. Thus, the scalar strain at the n^{th} cross-section is obtained by,

$$\begin{aligned}\varepsilon_{\mathrm{n,m}} &= \left\{S_{1_n} - \cos\sigma_{n,m} \cdot S_{6_n} + \sin\sigma_{n,m} \cdot S_{5_n}\right\}\cos\sigma_{n,m} \\ &\quad - \left\{S_{2_n} - \sin\sigma_{n,m} \cdot S_{4_n}\right\}\sin\mu_{n,m}\sin\sigma_{n,m} + \left\{S_{3_n} + \cos\sigma_{n,m} \cdot S_{4_n}\right\}\sin\mu_{n,m}\cos\sigma_{n,m}\end{aligned} \tag{16}$$

Therefore, the discretized form of Eq. (9) becomes,

$$\begin{bmatrix} \varphi_{\mathbf{n},\xi_1} \\ \mathbf{d}_{1_\mathbf{n},\xi_1} \\ \mathbf{d}_{2_\mathbf{n},\xi_1} \\ \mathbf{d}_{3_\mathbf{n},\xi_1} \end{bmatrix} = \begin{bmatrix} 0 & S_{1_n}+1 & S_{2_n} & S_{3_n} \\ 0 & 0 & \frac{S_{6_n}}{r} & -\frac{S_{5_n}}{r} \\ 0 & -\frac{S_{6_n}}{r} & 0 & \frac{S_{4_n}}{r} \\ 0 & \frac{S_{5_n}}{r} & -\frac{S_{4_n}}{r} & 0 \end{bmatrix} \begin{bmatrix} \boldsymbol{\varphi}_\mathbf{n} \\ \mathbf{d}_{1_\mathbf{n}} \\ \mathbf{d}_{2_\mathbf{n}} \\ \mathbf{d}_{3_\mathbf{n}} \end{bmatrix}. \tag{17}$$

We use a localized linear approach, linearizing the coefficient in Eq. (17) locally in each n^{th} segment, which is then solved analytically. We use the boundary and continuity condition to solve for the constants of integration. The midcurve position vector $\varphi_\mathbf{n}(\xi_1)$ and the directors $\mathbf{d}_{\mathbf{i_n}}(\xi_1)$ are obtained as Eq. (19) in [2]. In the next section, we demonstrate some application of the shape sensing algorithm to damage detection in underground pipelines.

3 Application to Damage Detection in Underground Pipelines

The underground pipelines are prone to severe damage due to seismic activities like earthquake, liquefaction- induced lateral spreading, landslide, and others. These events have global effect on the pipeline configuration. Hence, monitoring the performance of

underground pipelines during these seismic events and in real time is equally important as developing resilient design methodologies for the same.

Earthquakes causes transient ground deformation and permanent ground deformations. In the simplest sense, the primary cause of underground pipeline deformation is the movement of soil mass associated with the seismic activities. There is abrupt ground deformation at the margin of landslide.

The paper by O'Rourke et al. [10] describes a large-scale test conducted on high density polyethylene pipelines that were subjected to 1.22 m of strike-slip displacement at a vertical fault crossing an angle of 65°. We simulate a similar kind of pipe deformation except that we do it for a much longer circular pipeline of 500 m with a diameter of 800 mm. The schematic diagram of the strike-slip fault effecting the underground pipeline is shown in Fig. 2.

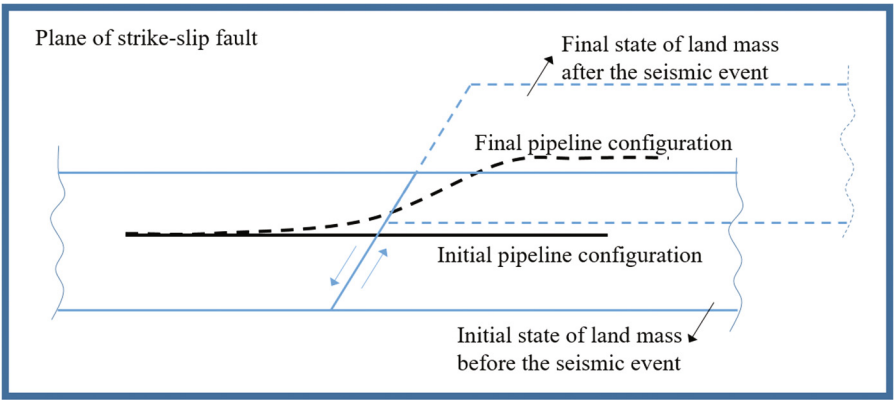

Fig. 2. Schematic diagram of strike-slip fault (Color figure online)

Since we ignore Poisson's effect, the algorithm is material-independent. We impart the pipeline with the axial strain shown in Fig. 3. We model the pipeline such that the left end is fixed. This represents the case where the portion of pipeline to the left of the considered portion is not effected by the seismic event. The scalar surface strain values for a given deformed shape at the set cross-sections for a strain gauge is obtained analytically using Eq. (15). The values of the strain parameters for the n^{th} section $\{S_{1_n}, \ldots, S_{6_n}\}$ (as required in Eq. (17)) is obtained by solving 6 simultaneous equations in Eq. (16). Note that if we include the Poisson's effect, we will have 7 unknown strain parameters. But excluding Poisson's effect simplifies the Eq. (16) to depend on $\{S_{1_n}, \ldots, S_{6_n}\}$. We fix the angles for 6 strain gauges at n^{th} cross-section as $\sigma_n = \left\{\frac{\pi}{4}, \frac{\pi}{2}, \frac{3\pi}{4}, \pi, \frac{5\pi}{4}, \frac{3\pi}{2}\right\}$ and $\mu_n = \left\{\frac{\pi}{4}, -\frac{\pi}{4}, \frac{\pi}{4}, -\frac{\pi}{4}, \frac{\pi}{4}, -\frac{\pi}{4}\right\}$. The set of angles σ_n and μ_n must be such that Eq. (16) is invertible.

The curvature is the dominant deformation for the pipeline with this geometric conditions. Hence, we primarily consider the deformation to consist of $\bar{\kappa}_2, \bar{\kappa}_3$, and the axial strain e. We run the simulation for 6 cases varying the number of equally spaced cross-sections N = (5, 10, 20, 50, 100), about which the strain gauges are attached.

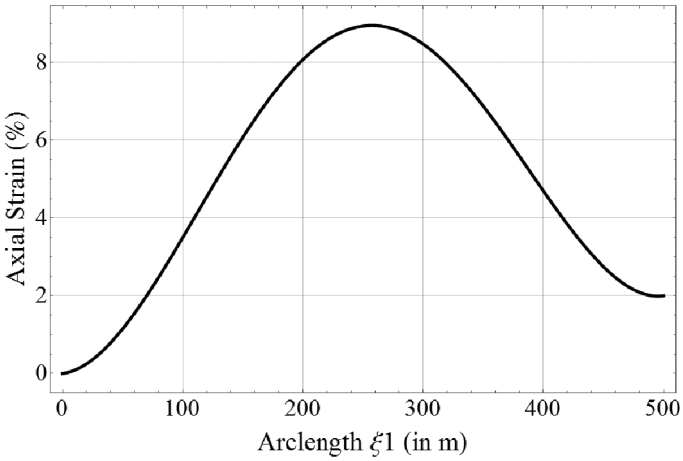

Fig. 3. Axial strain along the pipeline

Each section has 6 strain gauges. Hence there are $6N$ number of total strain gauges in the problem. The displacement of the distal end is $51.75\mathbf{E}_2 + 51.1\mathbf{E}_2$ (in m).

Figure 4 compares the reconstruction of the midcurve result (dotted black) for three cases of N = (5, 10, 100), with the exact deformed shape (orange). Figure 5 compares the reconstruction of the cross-sections by plotting the exact directors obtained using forward model ($\mathbf{d}_1$ in red, $\mathbf{d}_2$ in blue, $\mathbf{d}_3$ in green) with the directors predicted by the shape sensing algorithm (represented by dotted vectors). It is observed that the error is recognizable for 5 sensor locations (spacing of 100 m) with root mean error of 44 m. An excellent convergence is observed in the shape sensing with increase of sensor locations. For $N = 10$ and 100, the rms error is merely 2.354 and 0.015 m, respectively, which justifies an excellent shape reconstruction. Figure 6 compares the exact component of position vector of midcurve φ and the director $\mathbf{d}_1$ with the predicted components for N = 5, 10, and 50.

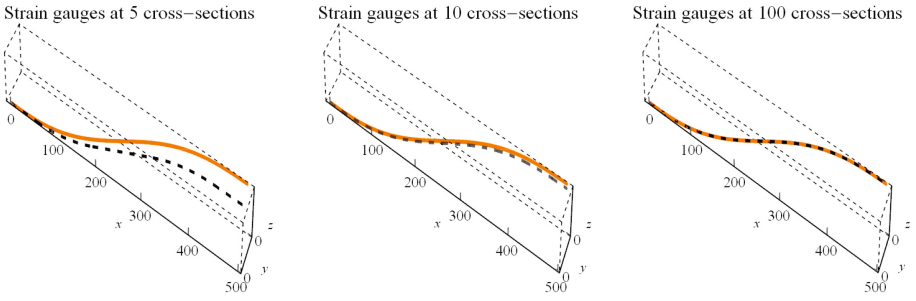

Fig. 4. Exact deformed shape (*orange curve*) of pipeline vs. the reconstructed shape of the pipeline (*dotted black*) (Color figure online)

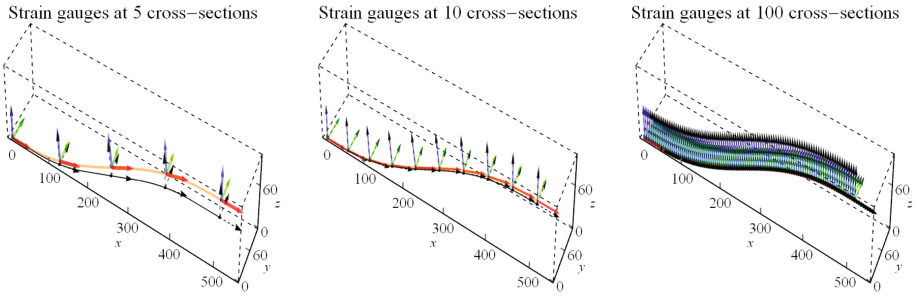

Fig. 5. Exact directors ($\mathbf{d}_1$ in *red*, $\mathbf{d}_2$ in *blue*, $\mathbf{d}_3$ in *green*) compared to the predicted directors (*dotted arrows*) (Color figure online)

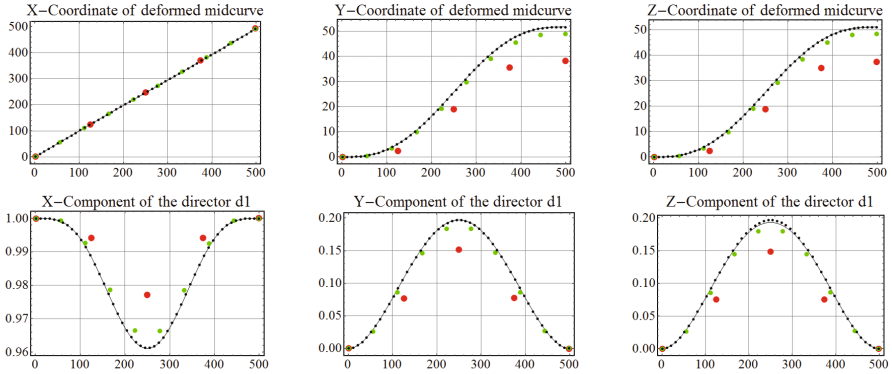

Fig. 6. Comparison of the component of exact (*solid black curve*) vectors $\boldsymbol{\varphi}$ and $\mathbf{d}_1$ with the predicted components for five, ten and fifty strain gauge locations (*red dot*, *green dot*, *black dot* respectively). (Color figure online)

In the ideal case, the strain gauge reading is noise-free. However, practicality dictates that an uncertainty/error analysis be performed, as real strain gages have noise. As in [1, 2], to examine these influences for a first-order assessment of robustness, we add uniformly distributed random noise to the strain values at a [−5, 5] microstrain level and at a [−50, 50] microstrain level before inputting these values into the shape sensing algorithm. We run fifty such realizations in the Monte-Carlo sense and evaluate the average rms error for different numbers of sensor counts. In fact there are three primary sources of error: the first is the error due to approximations in solving Eq. (17), the second is the error due to noisy strain gauge readings, and the third is the uncertainty in the boundary conditions. Figure 7 represents the average rms error for the position vector at various noise levels. The black curve represents the error for the no noise or the ideal case, where the primary cause of deviation is the approximations in the algorithm. The red and blue curves represent the error due to [−5, 5] and [−50, 50] microstrain noise, respectively. It is observed that the error depends on the noise level and the complexity of deformation. The error reduces at a rate greater than exponentially with the increase of sensor count.

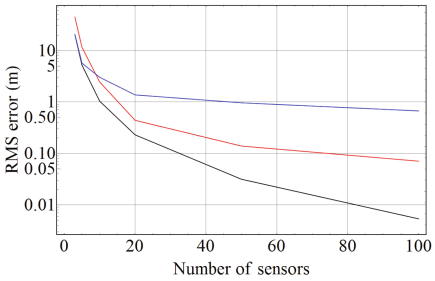

Fig. 7. Root mean square error for no noise (*black curve*), [−5, 5] micro strain noise (*red curve*) and [−50, 50] micro strain noise (*blue curve*) (Color figure online)

4 Conclusion

In this paper, we discussed about the shape sensing algorithm useful for the general three-dimensional shape reconstruction of slender structures. The problem bears the nature of a single manifold problem where the configuration of the structure is defined by the midcurve and the director triad. The methodology presented uses geometrically exact and nonlinear Cosserat rod theory, thereby making the method appropriate to capture large deformation involving finite strain. The formulation captures the effects due to elongation, shear, and curvatures $(e, \bar{\kappa}_1, \bar{\kappa}_2, \bar{\kappa}_3, \gamma_{11}, \gamma_{12}, \gamma_{13})$ assuming Euler-Bernoulli's rigid cross-section assumption.

We established the expression for the surface strain measure in terms of the strain parameters. The discretized form of the governing differential equations for the mid-curve position vector and director are obtained, and the global solution to the set of differential equations obtained is determined using the continuity conditions and the boundary conditions.

The primary purpose of this paper is to demonstrate the ability of this shape sensing methodology to monitor the deformed shape of underground pipelines, important for seismic monitoring applications. It is known that the underground pipelines are severely affected due to seismic activities like earthquake, landslide, and liquefaction.

We simulated a deformed shape for a portion of pipeline 500 m long and 800 mm in diameter and attempted to reconstruct its shape by our algorithm. Excellent reconstruction is obtained for as low as 10 sensor locations (50 m spacing, 60 sensors in total). We observed that the rms error decays with increase in sensor count. Therefore, the shape reconstruction method discussed above can serve as a useful aid in a damage detection strategy that involves knowing the displacement shifts in the pipeline.

References

1. Todd, M.D., Skull, C.J., Dickerson, M.: A local material basis solution approach to reconstructing the three-dimensional displacement of rod-like structure from strain measurements. ASME J. Appl. Mech. **80**, 041028 (2013). doi:10.1115/1.4023023

2. Chadha, M., Todd, M.D.: A generalized approach for reconstructing the three-dimensional shape of slender structures including the effects of curvature, shear, torsion and elongation. ASME J. Appl. Mech. **84**, 041003 (2017). doi:10.1115/1.4035785
3. Cosserat, E., Cosserat, F.: Theorie des Corps Deformable. Herman, Paris (1909)
4. Simo, J.C.: A finite strain beam formulation. The three-dimensional dynamic problem. Part 1. Comput. Methods Appl. Mech. Eng. **49**, 55–70 (1985)
5. Simo, J.C., Vu-Quoc, L.: A geometrically exact rod model incorporating shear and torsion-warping deformation. Int. J. Solids Struct. **27**, 371–393 (1991)
6. Iura, M., Atluri, S.N.: On a consistent theory, and variational formulation of finitely stretched and rotated 3-d space-curved beam. Comput. Mech. **4**, 73–88 (1989)
7. Reissner, E.: On one-dimensional finite-strain beam theory: the plane problem. J. Appl. Math. Phys. **23**, 795–804 (1972)
8. Reissner, E.: On one-dimensional large displacement finite beam theory. Stud. Appl. Mech. **52**, 87–95 (1973)
9. Reissner, E.: On finite deformation of space curved beams. J. Appl. Math. Phys. **32**, 734–744 (1981)
10. O'Rourke, T.D., Jung, J.K., Argyrou, C.: Underground pipeline response to earthquake-induced ground deformation. Soil Dyn. Earthq. Eng. **91**, 272–283 (2016)